Quality Factor Improvement of a TPoS Resonator by Using a Radial Alternating Materials Phononic Crystal

Chuang Zhu , Muxiang Su , Temesgen Bailie Workie , Panliang Tang , Changyu Ye , Jing-Fu Bao *

Posted Date: 24 November 2023

doi: 10.20944/preprints202311.1597.v1

Keywords: RAM-PnC; resonator; anchor loss

Article

Quality Factor Improvement of a TPoS Resonator by Using a Radial Alternating Materials Phononic Crystal

Chuang Zhu , Muxiang Su , Temesgen Bailie Workie , Panliang Tang , Changyu Ye , Jing-Fu Bao *

Posted Date: 24 November 2023

doi: 10.20944/preprints202311.1597.v1

Keywords: RAM-PnC; resonator; anchor loss

Article

Quality Factor Improvement of a TPoS Resonator by Using a Radial Alternating Materials Phononic Crystal

Chuang Zhu, Muxiang Su, Temesgen Bailie Workie, Panliang Tang, Changyu Ye and Jing-Fu Bao *

School of Electronic Science and Engineering, University of Electronic Science and Technology of China,Chengdu 611731, China; Zc20082012@163.com (C.Z.); 202322310701@std.uestc.edu.cn (M. S.); wtbailie@std.uestc.edu.cn (T.B.W.); mailfortpl@163.com (P.T.); yechangyu@std.uestc.edu.cn (C.Y.)
* Correspondence: baojingfu@uestc.edu.cn (J.B.)

Abstract: This paper proposes a radial alternating materials phononic crystal (RAM-PnC). By simulating the band gap structure of the phononic crystal, it is verified that there is a complete acoustic band gap at the resonant frequency of 175.14 MHz, which can prevent the propagation of elastic waves in a specific direction. The proposed alternately arranged radial phononic crystal structure is applied to the thin-film piezoelectric-on-silicon (TPOS) MEMS resonator. The finite element simulation method increases the anchor quality factor (Q_{anchor}) from 60596 to 659536011 at the operating frequency of 175.14 MHz, which is about 10,000 times higher. The motion resistance of the RAM-PnC resonator is reduced from 156.25 Ω to 48.31 Ω compared with the traditional resonator. At the same time, the insertion loss of the RAM-PnC resonator is reduced by 1.1 dB compared with the traditional resonator.

Keywords: RAM-PnC; resonator; anchor loss

1. Introduction

Radiofrequency microelectromechanical system (RF-MEMS) is an essential branch of MEMS technology. The advantages of RF-MEMS devices, such as low power consumption, miniaturization, and integration with CMOS (Complementary Metal Oxide Semiconductor) circuits, are urgently needed in future RF communication systems. With the advent of the 5G era, a mobile phone needs to meet all the communication bands of 3G, 4G, and 5G at the same time, as well as Bluetooth, Wi-Fi and GPS, so the number of filters in the mobile phone terminal will be greatly increased to about 100. Therefore, various RF front-ends have an urgent need for filters with small sizes, low power consumption and high performance [1]. As the core of the filter, the size, power consumption and performance of the resonator have an essential influence on the index of the filter. Many researchers have done a lot of work to improve its performance and quality factor [2–4].

In 2011, B P Harrington and R Abdolvand [5] introduced an acoustic mirror structure that can reflect the elastic waves propagating from the resonator, and the *Q* enhancement is as high as 560 %. In 2016, Joshua E.-Y. Lee et al. [6] changed the displacement distribution on the resonant body by optimizing the structure of the resonant body itself to minimize the vibration at the support beam, thereby reducing the acoustic wave dissipated outward through the support beam. In 2017, Li Enyuan et al [7] proposed a stress-release hole structure, and the hole redistributes the strain energy in the resonant cavity. The redistribution of strain energy significantly inhibits the axial deformation of the support beam anchor cable and destroys the anchorage zone. Reducing the anchor cable's energy and the anchorage area can reduce the anchorage loss and improve *Q*.

In 2017, Jie Zou, Chih-Ming Lin, et al. [8] proposed a butterfly aluminum nitride (AlN) plate with an anchor plate angle of less than 90°.By eliminating the anchor point loss and improving the quality factor (*Q*) of the LWRs resonator, the circular butterfly plate has a better suppression effect

 doi:10.20944/preprints202311.1597.v1

on the anchor loss than the inclined butterfly plate. In addition, the emerging phononic crystal theory and technology in recent years have greatly improved the performance of MEMS resonators. In previous studies, many types of phononic crystals have been proposed, such as hole circles, air holes [9], rings [10], solid-disks [11], cross-shape [12], Spider Web-Like shapes [13] ,and so on [14–21,27]. However, it is relatively rare to use radial phononic crystals to improve the quality factor of resonators. Therefore, this paper discusses the effect of radial phononic crystals on the performance of MEMS resonators.

Theoretical analysis of phononic crystals (PnC) is a novel class of periodic synthetic materials that can be used to manipulate the propagation of elastic waves and acoustic waves [28]. Based on traditional phononic crystals, some researchers have proposed radial phononic crystal structures, which are arranged periodically in the radial direction and will play a huge advantage under certain circumstances. Torrent et al. [29–31] studied the propagation characteristics of body waves in radial phononic crystal and found that the propagation of radial body waves in a specific frequency band is prohibited. Li et al. [32] and Ma et al. [33] constructed two types of radial phononic crystals, and studied the propagation characteristics of Lamb waves in them. In 2015, Shu Hai-Sheng [34] proposed a generalized phononic crystal one-dimensional cylindrical shell (CS GPCs) in which two homogeneous materials are periodically arranged along the radial direction, and its 1D CS GPCs can also have radial, torsional shear and axial shear wave band gaps in the high- frequency region that conform to the Bragg scattering effect. In 2016, Xiaona Shi, Haisheng Shu, et al. [35] proposed that two alternate homogeneous materials are periodically introduced along the radial direction to form a circular plate of radial phononic crystals (CPRPC). Radially periodic, there are significant transverse and longitudinal wave band gaps. In 2018, Yinggang Li et al [32] proposed a composite radial plate-type elastic metamaterial composed of periodic double-sided composite branches on a one-dimensional binary radial phononic crystal plate. In 2018, Shuowei An, Haisheng Shu et al. [36] proposed a two-dimensional cylindrical shell structure with radial and circumferential periods. Through the calculation and discussion of wave transmission characteristics, it is found that the radial wave in the design shows apparent attenuation in a particular frequency region, that is, the wave band gap.

Based on the work and research of the above researchers, this paper first proposes the RAM-PnC structure. Combining Si and metal W into a multi-material design has a wide band gap range and avoids the strength damage of the etched substrate to the resonator anchor point. Then, the proposed structure's dispersion and transmission curves are calculated, and the effects of different materials and structural parameters on the band gap are discussed. Finally, it is applied to the TPOS MEMS resonator designed in this paper, significantly improving its performance.

2. Phononic Crystal & Theory of Wave Propagation

2.1. Phononic crystal structure and band gap calculation

As shown in Figure 1, we constructed a three-dimensional schematic diagram of a one-dimensional radial phononic crystal composed of two alternating materials (green represents W, gray represents silicon). In Figure 1, the radial phononic crystal cylindrical shell is a one-dimensional cylindrical semi-infinite periodic structure formed by two kinds of solid dielectric materials, W and Si, with different elastic constants and densities in the r direction. The width a_1 of the W layer is 6 μm, the width a_2 of the Si layer is 10 μm, and the height of the W layer and the Si layer is H = 10 μm. A radial periodic unit is alternately formed by W and Si, and its length is a = 16 μm. Silicon is an anisotropic material, and its crystal orientation and elastic coefficient influence the simulation results. In this paper, the parameters of silicon are the crystal orientation, and the elastic coefficients are shown in Table 1.

 doi:10.20944/preprints202311.1597.v1

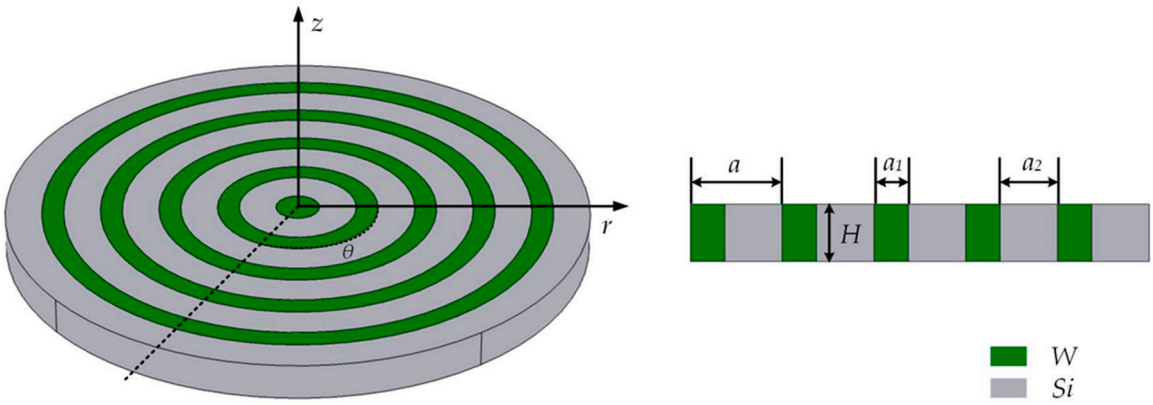

Figure 1. RAM-PnC three-dimensional schematic diagram and cross-section diagram.

Table 1. The specific parameters of silicon set by simulation in this paper.

Parameter name (abbreviated)	Value
Young 's modulus (E)	E_x=E_y=169 GPa, Ez=130 GPa
Poisson's ratio (σ)	σ_{xy}=0.064, σ_{yz}=0.36, σ_{zx}=0.28
Shear modulus (G)	Gz=50.9 GPa, Gx=Gy=79.6 GPa
Density (ϱ)	2330 kg/m^3

$$\rho\frac{\partial^2 u}{\partial t^2}=(\lambda+2\mu)\frac{\partial\theta_t}{\partial r}-\frac{2\mu}{r}\frac{\partial w_z'}{\partial\theta}+2\mu\frac{\partial w_\theta'}{\partial\theta} \tag{1}$$

$$\rho\frac{\partial^2 v}{\partial t^2}=(\lambda+2\mu)\frac{\partial\theta_t}{\partial r}-2\mu\frac{\partial w_z'}{\partial\theta}+2\mu\frac{\partial w_r'}{\partial r} \tag{2}$$

$$\rho\frac{\partial^2 w}{\partial t^2}=(\lambda+2\mu)\frac{\partial\theta_t}{\partial z}-\frac{2\mu}{r}\frac{\partial w_z'}{\partial\theta}+\frac{2\mu}{r}\frac{\partial w_r'}{\partial\theta} \tag{3}$$

Where u, v, and w are displacements, ρ is mass density, t is time, λ and μ are Lame constants, and r, θ and z represent coordinate variables in cylindrical coordinates, respectively. In addition, the volume strain and the rotational component are defined as the following formulas.

$$\theta_t=\frac{1}{r}\frac{\partial(ru)}{\partial r}+\frac{1}{r}\frac{\partial u}{\partial\theta}\frac{\partial w}{\partial r} \tag{4}$$

$$w_r'=\frac{1}{2}\left(\frac{1}{r}\frac{\partial w}{\partial\theta}+\frac{1}{r}\frac{\partial v}{\partial z}\right) \tag{5}$$

$$w_\theta'=\frac{1}{2}\left(\frac{1}{r}\frac{\partial u}{\partial\theta}+\frac{\partial w}{\partial r}\right) \tag{6}$$

$$w_z'=\frac{1}{2}\left(\frac{1}{r}\frac{\partial(rv)}{\partial\theta}+\frac{\partial u}{\partial\theta}\right) \tag{7}$$

COMSOL Multiphysics solved the intrinsic equation (1) - (4). In the stress-strain application model, the displacement v and the stress and strain components in the direction are assumed to be 0. In this model, the displacement u_{or} and z are defined. The dependent variable $u_{or}\equiv u / r$ is introduced to avoid dividing r, leading to axis problems. In equations (4) - (7), r = 0, w is the displacement in z direction. Periodic boundary conditions are imposed on the element in the r direction:

$$\mu(r+r_a,z)=\mu(r,z)e^{ik_r r_a} \tag{8}$$

Where r is the radial position, a is the lattice constant, and the parameter kr is defined as a one-dimensional block wave vector along the radial direction. The free boundary is applied to the plate

 doi:10.20944/preprints202311.1597.v1

surface along the z direction. By scanning the wave vector kr along the boundary of the first Brillouin zone, the dispersion curve $\omega = \omega(k)$ and the eigen-displacement field can be obtained. The structure used in this section is one-dimensional in the radial direction, so the Brillouin zone boundary ranges from Γ (0,0) to R (1,0), which is different from the two-dimensional or three-dimensional phononic crystal structure.

2.2. Band gap optimization of phononic crystals

Different materials will affect the band gap of the structure. Mass density and Young's modulus are two main factors to adjust the band gap for solid-solid phononic crystals. Damping materials consider six common metals: W, Al, Ag, Pt, Cu, and Au. Detailed material parameters are shown in Table 2. By comparing the acoustic parameters in the table, we find that the acoustic impedance of metal W is the largest. Furthermore, we simulated the dispersion curves of different materials in the frequency range of 0-280 MHz. Figure 2a shows the wide band gap of 122 MHz-225 MHz. Figure 2b is metal Al, and its band gap range is 198 MHz-218 MHz. Figure 2c represents the metal Ag, and its band gap ranges are 165 MHz-171 MHz, 231 MHz-237 MHz and 238 MHz-242 MHz. Figure 2d represents metal Pt, and its band gap ranges are 110 MHz-141.5 MHz, 156 MHz-170 MHz, 172 MHz-183 MHz, 228.5 MHz-238.5 MHz and 247 MHz-263 MHz. Figure 2e represents the metal Cu with a band gap range of 158 MHz-177 MHz. Figure 2f represents the metal Au, and its band gap range is 120 MHz-136.5 MHz, 168 MHz-175 MHz, 192 MHz-208 MHz, 227 MHz-234 MHz, 250 MHz-255 MHz, 262 MHz-272 MHz, 273.5 MHz-277.5 MHz. By comparing the band gap range generated by the combination of the above six metals and Si, the combination of W and Si has the best effect, which has a wider band gap width and thus has an excellent acoustic isolation effect.

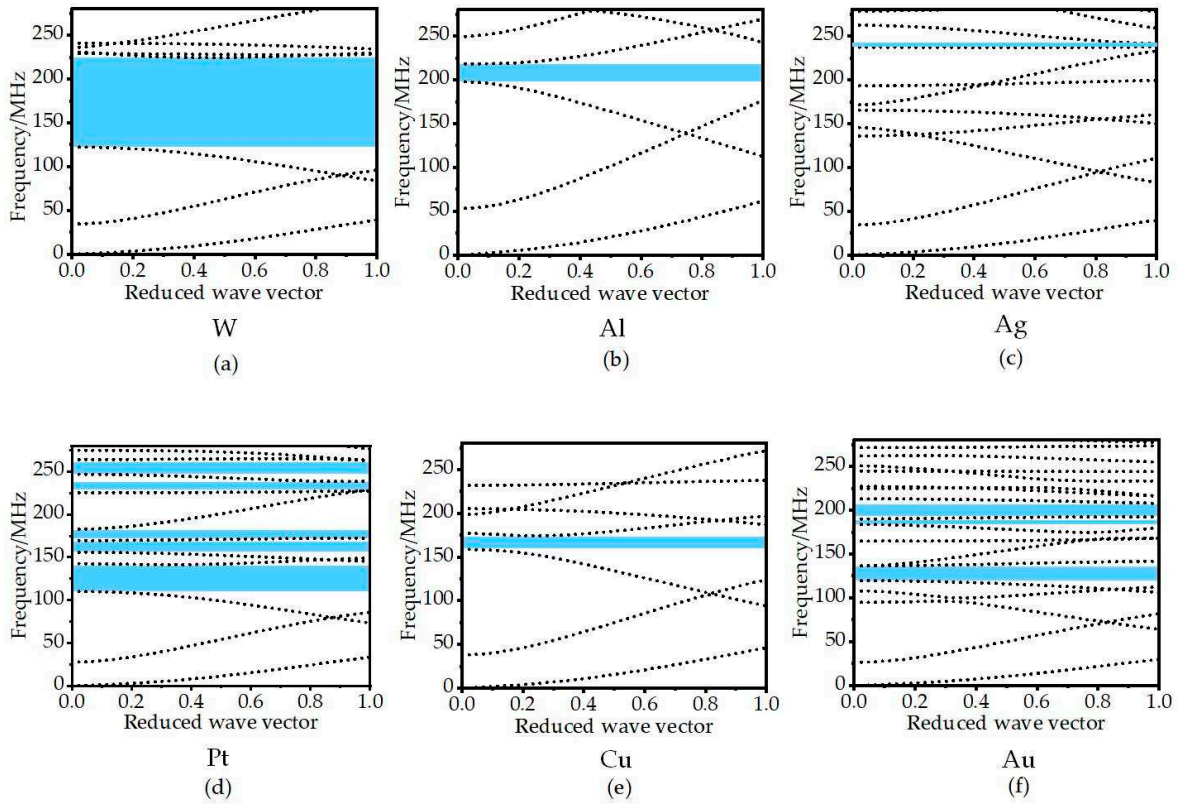

Figure 2. Dispersion curves formed by different metal materials combined with Si.

 doi:10.20944/preprints202311.1597.v1

Table 2. Characteristic parameter table of different metals.

Materials	W	Al	Ag	Pt	Cu	Au
Density (g/cm²)	18.7	2.7	10.5	21.4	8.94	19.32
Longitudinal velocity (cm/s) ×10²	5.23	6.32	3.6	3.96	4.65	3.24
Acoustic impedance (g/cm²s)	97.86	17.1	37.8	84.74	41.55	62.6

The band gap range is further analyzed when other parameters are kept unchanged and only the metal width w is changed. The calculation results are shown in Figure 3. It can be seen from the figure that when the metal width w gradually increases from 2 μm to 30 μm, the initial band gap and the final band gap of the first band gap decrease, and the band gap becomes wider and narrower. When the metal width w = 6 μm, the widest band gap of 122-225 MHz is obtained.

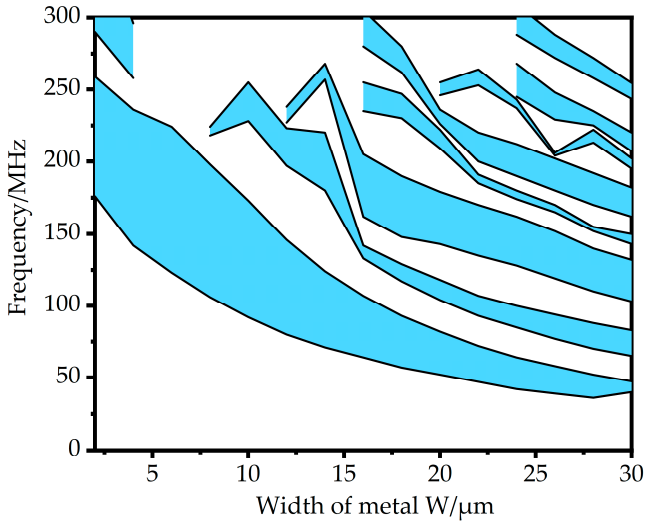

Figure 3. Dispersion curves formed by different metal materials combined with Si.

2.3. Transmission characteristic

By calculating the elastic wave transmission curve, the existence and ability of the proposed RAM-PnC acoustic band gap are evaluated. Different from the infinite scattering array used for dispersion relation, the model used for transmission spectrum analysis is a finite scattering array. As shown in Figure 4, there are five periodic units arranged alternately in the radius direction. A is the excitation port, B is the receiving port, and the outermost layer is the PML layer with a length of 5a. The transmission loss is defined by the following equation:

$$S_{21} = 10log_{10}\left(\frac{P_{out}}{P_{in}}\right) = 10log_{10}\left(\frac{d_{out}^2}{d_{in}^2}\right) \quad (9)$$

The harmonic excitation of the radial displacement in the direction of R is applied to the inner ring of RAM-PnC, represented by din, to excite the radial wave propagating from the inner ring to the outer ring, as shown in the figure. In order to eliminate the reflection effect of the outer boundary, the outer circle is surrounded by a perfectly matched layer (PML). It is assumed that there are good bonding conditions at the interface between materials.

 doi:10.20944/preprints202311.1597.v1

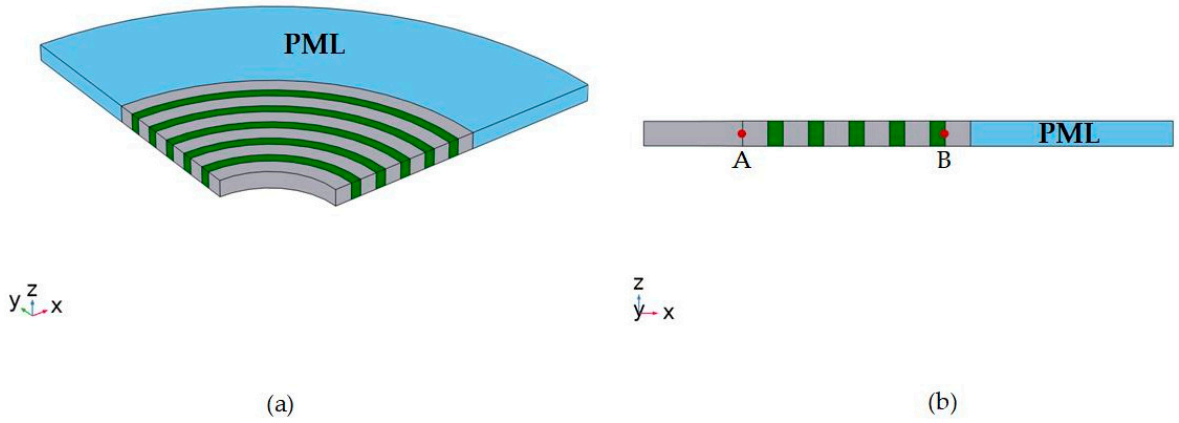

Figure 4. The 5-period radial RAM-PnC transmission line model.

The transmission characteristics of the phononic crystal array obtained by the delay line model are calculated in the frequency range of 0-300 MHz, as shown in Figure 5. The band gap is formed in the range of 122-225 MHz, and the propagation of acoustic wave is well suppressed. As shown in Figure 5a, under the condition of two-dimensional simulation, the acoustic waves suppression ability reduces the acoustic wave transmission coefficient by 60 dB at a frequency of 175.14 MHz. As shown in Figure 5b, under the condition of three-dimensional simulation, the acoustic wave suppression ability reduces the acoustic wave transmission coefficient by 45 dB at a frequency of 175.14 MHz.

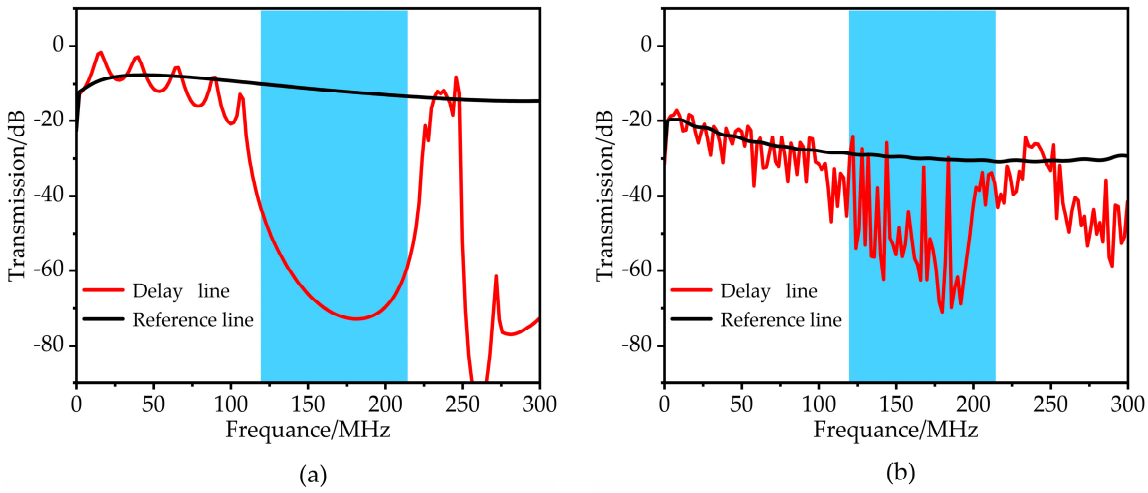

Figure 5. The simulation results of RAM-PnC transmission curve (122MHz-225MHz) under the conditions of 2D (a) and 3D (b), respectively.

3. The design of TPOS resonator

Figure 6 shows the three-dimensional structure diagram of the resonator designed in this paper. The resonator structure is composed of three layers of materials. From top to bottom, the metal aluminum with a thickness of 0.5 m as the upper electrode, the AlN piezoelectric film with a thickness of 0.1 μm and the bottom silicon structure layer with a thickness of 10 μm is used as the lower electrode of the resonator. Applying a voltage to the metal upper electrode generates a vertical electric field between the metal upper electrode and the silicon structure layer as the lower electrode on the piezoelectric film. Due to the inverse piezoelectric effect of the piezoelectric material, according to the d31 piezoelectric coefficient of the AlN material, the electric field causes the plane expansion deformation of the piezoelectric film, thereby exciting the resonator to cause lateral expansion mode resonance.

Preprints.org (www.preprints.org) | NOT PEER-REVIEWED | Posted: 24 November 2023 doi:10.20944/preprints202311.1597.v1

The top view of the resonator designed in this paper is shown in Figure 7, which clearly shows the characteristics of the designed resonator: phononic crystals composed of radial alternating materials. A reflective structure is added to the support beam to constrain more energy in the resonator. The structure is divided into a multi-layer periodic structure with alternating high and low equivalent acoustic impedance. When the acoustic wave transmitted from the resonator passes through the reflection block, the acoustic wave will be reflected at the interface between the periodic structural layers. Part of the energy transmitted to the reflection block will be reflected to the resonator, which suppresses the energy loss of the resonator to a certain extent, thereby improving the Q value of the device. Figure 6b shows the schematic diagram of the reflective structure with alternating materials. The structural parameters of the designed resonator are marked in Figure 7. The detailed parameters are listed in Table 3.

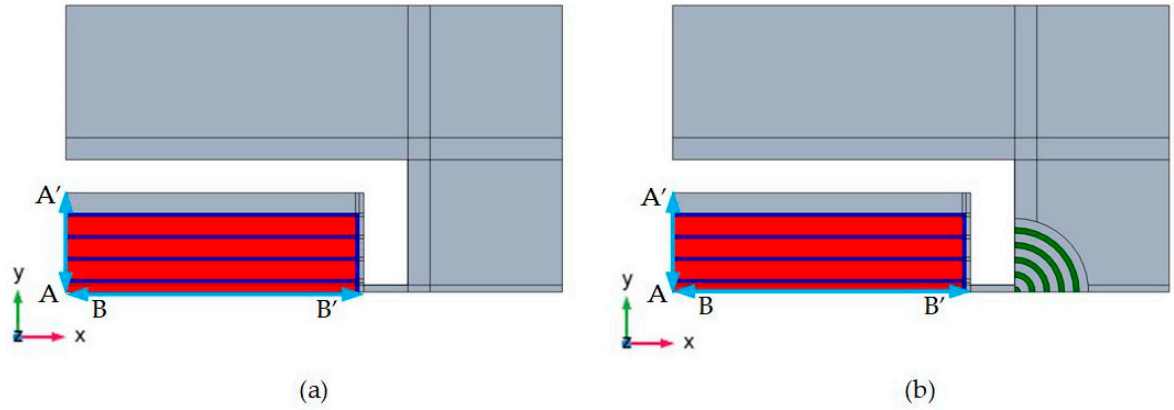

Figure 6. Simulation diagrams of quarter piezoelectric MEMS resonators: (a) traditional type TPOS MEMS resonator; (b) RAM-PnC TPOS MEMS resonator.

The simulation model is shown in Figure 6. Since the overall structure of the resonator is symmetrical, only a quarter of the model can be established in order to reduce the amount of calculation during simulation. The simulation of the complete model can be equivalent by assigning ' symmetrical ' boundary conditions to the symmetrical surface. In addition, a perfect matching layer needs to be set on the periphery of the resonator to absorb the elastic waves propagating outward to avoid the influence of elastic wave reflection on the simulation results. The width of the perfect matching layer is generally set to three times the wavelength so that it can fully absorb the elastic waves propagating out.

Table 3. The specific size parameters of the resonators.

Parameters	Values (unit)
Simulated resonant frequency (f_0)	175 (MHz)
Wave length (λ)	47.9 (μm)
Inter digitated transducer (IDT) finger (n)	9
Tethers Width (W_t)	15 (μm)
Tethers Length (L_t)	47.9 (μm)
Electrode gap (G_e)	4 (μm)
Resonator width (W_r)	215.55 (μm)
Resonator length (L_r)	646.65 (μm)
Thickness of Al (T_{Al})	0.5 (μm)
Thickness of AlN (T_{AlN})	0.1 (μm)
Height of silicon substrate (HS)	10 (μm)

The above two resonators were modeled and simulated by using the finite element simulation software COMSOL Multiphysics to study the properties of their 9-order lateral expansion modes, as

 doi:10.20944/preprints202311.1597.v1

shown in Figure 6. The order of the resonator is set to nine. Therefore, the width of the resonator is 215.55, and the length is three times the width of 646.65. In the design of the device, the wavelength (i.e., λ) corresponding to the acoustic wave at the operating frequency of the resonator is designed to be twice the width of the adjacent interdigital electrode. Based on this, the following formula calculates the mechanical resonance frequency of the device:

$$f_0 = \frac{v_p}{\lambda} = \frac{n}{2L}\sqrt{\frac{E}{\rho}} \tag{10}$$

Where v_p is the phase velocity associated with the lateral spreading mode, E and ρ denote the Young's modulus and density of the silicon layer, respectively, n. It is the order of the resonant mode.

The mode of the resonator obtained by simulation is shown in Figure 7. Figure 7a shows the total displacement distribution of the 9-order broadened resonance mode of the traditional resonator. Figure 7b shows the total displacement distribution of the 9th-order stretched resonant mode of the RAM-PnC resonator. Figure (c) shows the Z-direction displacement distribution of the 9th-order stretched resonant mode of the ordinary resonator. Figure (d) shows the Z-direction displacement distribution of the 9th-order stretched resonant mode of the RAM-PnC resonator. The simulation results show that integrating the RAM-PnC array on the resonator can increase the resonator's quality factor from 60596 to 659536011.

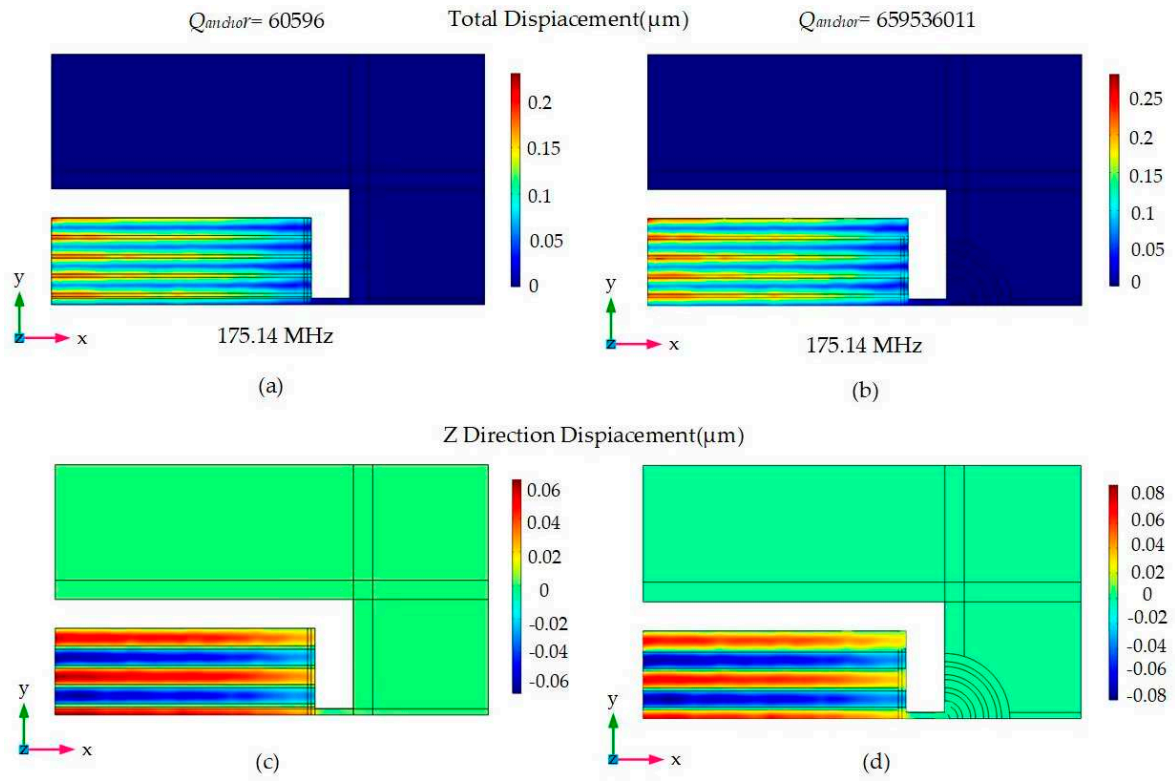

Figure 7. The total displacement distribution of the 9th-order width-extended resonant mode of (a) ordinary resonator and (b) array plate resonator with RAM-PnC is shown in the figure; the Z-direction displacement distribution of the 9th-order width-extended resonant mode of (c) ordinary resonator and (d) array plate resonator with RAM-PnC is shown in the figure.

In addition, by comparing the maximum vibration amplitude of the two resonators, it is shown that the integration of the RAM-PnC array on the resonator can concentrate more acoustic waves in the resonator, so the amplitude on the resonator is more significant, and the performance of the resonator is better. To quantitatively analyze the anchor loss of the substrate, the total displacement and Z-direction displacement at the A-A ' and B-B ' intercepts on the substrate are extracted, as shown in Figure 8. From Figure 8a–d, it can be seen that the integration of RAM-PnC array on the resonator

 doi:10.20944/preprints202311.1597.v1

is more effective in suppressing the anchor loss. The maximum total displacement at the A-A ' cross-section is increased from 0.194 μm to 0.248 μm, and the maximum Z-direction displacement at the A-A ' cross-section is increased from 0.06 μm to 0.075 μm. The maximum total displacement at the B-B ' intercept is increased from 0.169 μm to 0.208 μm, and the maximum Z-direction displacement at the B-B ' intercept is increased from 0.017 μm to 0.0215 μm.

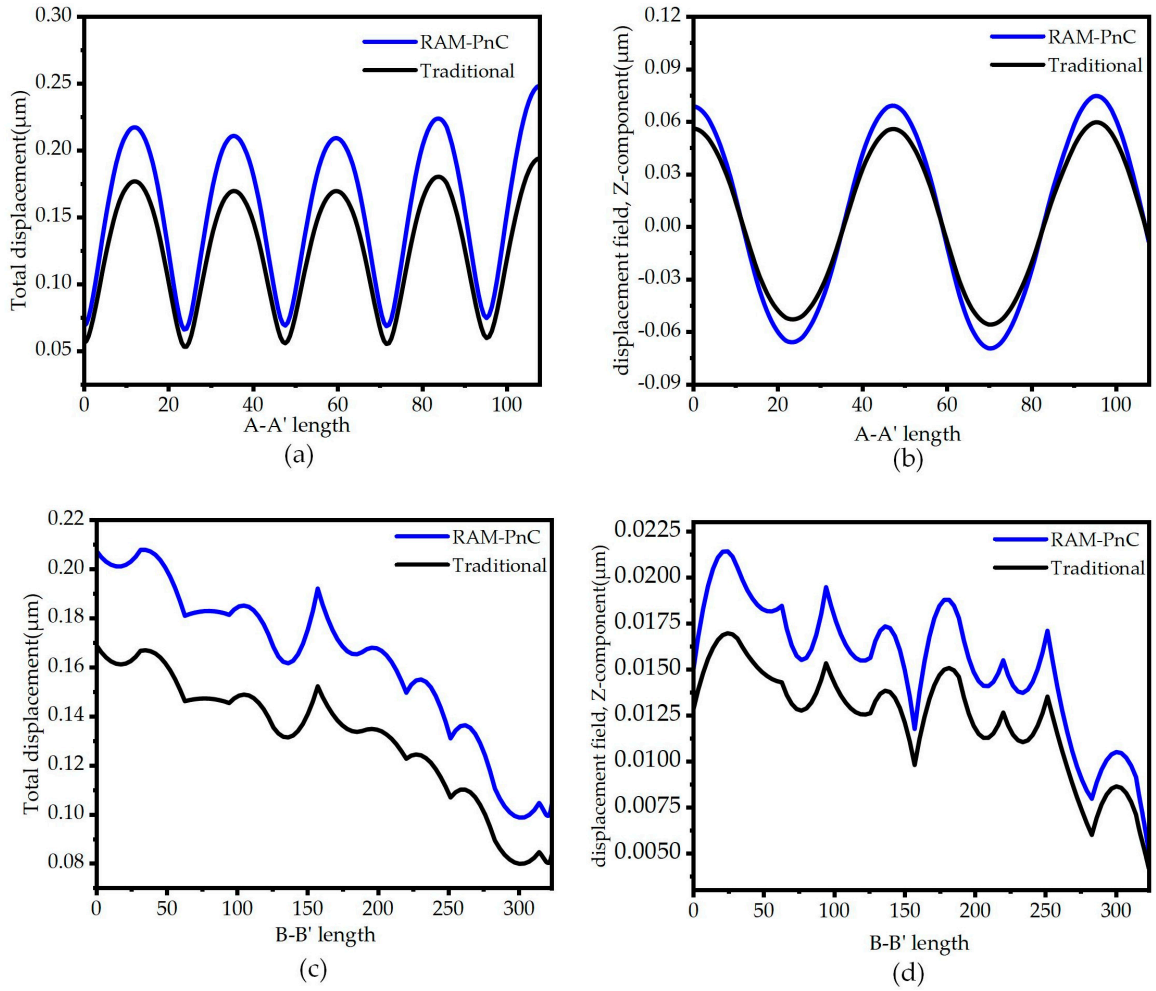

Figure 8. The (a) total displacement field (μm) diagram and (b) Z-direction displacement field (μm) diagram of the traditional resonator and the RAM-PnC resonator in the 9th-order width extension mode on the A-A' cross-section, and the (c) total displacement field (μm) diagram and (d) Z-direction displacement field (μm) diagram of the traditional resonator and the RAM-PnC resonator in the 9th-order width extension mode on the B-B ' crossp-section.

4. Discussion

To further obtain the equivalent circuit parameters of the resonator, the frequency domain simulation of the resonator based on 50-ohm impedance matching is carried out by the finite element method, and the Y11 curve and S21 curve are obtained, respectively. The simulation results are shown in Figures 9 and 10. From Eq. (11) to Eq. (14), the various parameter values of the piezoelectric MEMS resonator are solved. Since there is no load in the simulation process, the no-load quality factor (Q_u) can be obtained by calculating the 3dB bandwidth.

$$Q_l = \frac{f_s}{\Delta f_{-3dB}} \tag{11}$$

 doi:10.20944/preprints202311.1597.v1

$$Q_u = \frac{Q_l}{1 - 10^{-\frac{IL}{20}}} \tag{12}$$

$$R_m = \frac{1}{\max\{Re(Y11)\}} \tag{13}$$

$$K_{eff}^2 = \frac{f_p^2 - f_s^2}{f_p^2} \tag{14}$$

Where $\triangle f_{\text{-3dB}}$ is −3 dB bandwidth, and IL is insertion loss, max {Re(Y11)} is the maximum real part of admittance, f_p is the frequency at which the impedance amplitude is maximum, and f_s is the frequency when the impedance amplitude is the minimum.

The Figure of Merit (FoM) values between resonators can be compared to measure the performance of MEMS resonators. The definition of piezoelectric resonator figure of FoM is proportional to Q and coupling factor. The calculation formula is as follows :

$$FoM = k_{eff}^2 * Q \tag{15}$$

The above analysis and calculation compare the specific performance parameters of the traditional resonator and the RAM-PnC resonator at 175.14 MHz. The particular performance parameters obtained by simulation in this paper are summarized in Table 4.

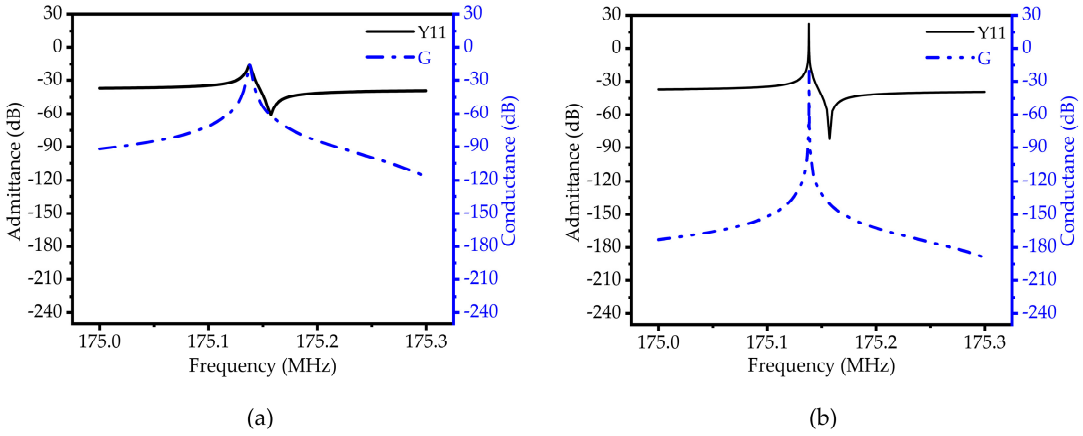

Figure 9. (a) Schematic diagram of admittance (Y11) and susceptance (G) curves of traditional TPOS MEMS resonators ; (b) RAM-PnC MEMS resonator admittance (Y11) and susceptance (G) curve diagram.

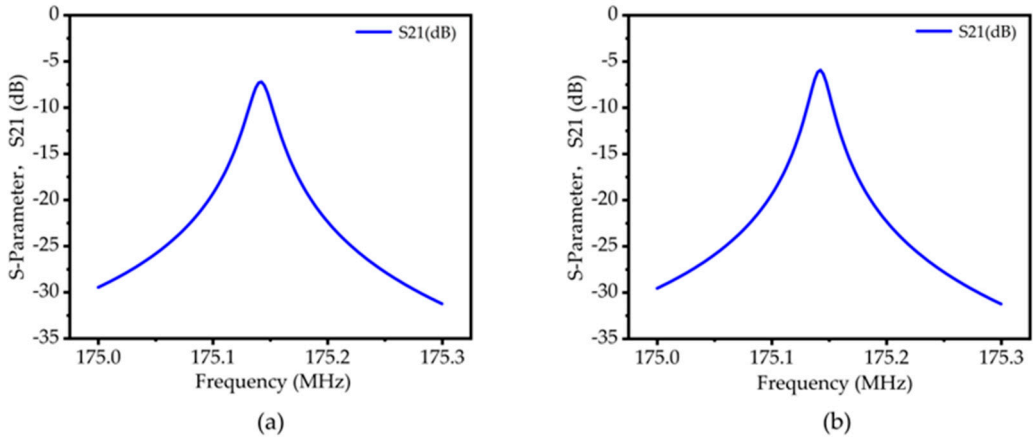

Figure 10. (a) Insertion loss (S21) curve of traditional TPOS MEMS resonator ; (b) Insertion loss (S21) curve of RAM-PnC TPOS MEMS resonator.

 doi:10.20944/preprints202311.1597.v1

Table 4. Summary of the simulated result.

Parameters	Traditional	RAM-PnC
Resonant frequency (f_r), MHz	175.14	175.14
Insertion Loss (IL), dB	6.2	5.1
Motional resistance (Rm), Ω	6.45	0.08
Coupling coefficient (K^2_{eff}), %	0.0228	0.0228
Q_{anchor}	60596	659536011
Loaded Quaity factor (Q_l)	8146	9467
Unloaded Quality factor (Qu)	15966	21317
FOM	8.3	11.1

5. Conclusions

In this paper, a RAM-PnC structure is proposed. The finite element simulation method is used to calculate the dispersion curve and frequency response curve. The results show that RAM-PnC has a complete band gap width between 122-225 MHz, which can isolate elastic waves well. Then, the influence of different metal materials on the band gap is studied. By combining six kinds of metal materials (W, Al, Ag, Pt, Cu, Au) commonly used in MEMS with Si, it is found that the multi-material radial phononic crystal plate containing metal W produces the widest band gap. Generally, the wide band gap has better performance in preventing wave propagation, so the metal W is selected. Then, the optimal band gap structure is obtained by adjusting the width of the metal material W. Finally, RAM-PnC is implanted into the piezoelectric MEMS resonator, and the anchor quality factor is increased from 60596 to 659536011. The dynamic impedance is reduced from 6.45 Ω to 0.08 Ω. The merit value (FoM) increased from 8.3 to 11.1.

Author Contributions: Conceptualization, C.Z., M.S. and J.B.; methodology, C.Z.; software, C.Z.; validation, C.Z., M.S and J. B.; formal analysis, C.Z.; investigation, C.Z., P.T., C. Y. and J.B.; resources, T.B.W. and J. B.; data curation, C.Z.; writing—original draft preparation, C.Z.; writing—review and editing, C.Z.; visualization, C.Z.; supervision, J. B.; project administration, J. B.; funding acquisition, J. B. All authors have read and agreed to the published version of the manuscript.

Funding: This work is supported in part by the research project under grant A1098531023601318 and in part by the grant from the National Natural Science Foundation of China and the China Academy of Engineering Physics under grant U1430102.

Conflicts of Interest: The authors declare no conflict of interest.

References

1. G. Hueber, J. Tesutsumi, M. Seth, et al. Cost-Efficient, High-Volume Transmission[J]. *Microwave Magazine*, 2015, 16(7): 26-45
2. Workie, T.B.; Wu, Z.; Tang, P.; Bao, J.; Hashimoto, K.Y. Figure of Merit Enhancement of Laterally Vibrating RF-MEMS Resonators via Energy-Preserving Addendum Frame. *Micromachines* 2022, 13, 105.
3. Piazza, G.; Stephanou, P.J.; Pisano, A.P. Piezoelectric Aluminum Nitride Vibrating Contour-Mode MEMS Resonators. *J. Microelectromech. Syst*. 2006, 15, 1406–1418.
4. Awad, M.; Workie, T.B.; Bao, J.; Hashimoto, K.-y. Nonconventional Tether Structure for Quality Factor Enhancement of Thin-Film-Piezoelectric-on-Si MEMS Resonator. *Micromachines* 2023, 14, 1965.
5. B. P. Harrington, R. Abdolvand. In-plane acoustic reflectors for reducing effective anchor loss in lateral–extensional MEMS resonators[J]. *Journal of Micromechanics & Microengineering*, 2011, 21(8): 085021.
6. C. Tu, J. E. -Y. Lee. VHF-band biconvex AlN-on-silicon micromechanical resonators with enhanced quality factor and suppressed spurious modes[J]. *Journal of Micromechanics & Microengineering*, 2016, 26(6): 065012.
7. C. Tu, J. E. -Y. Lee. Enhancing quality factor by etch holes in piezoelectric-on-silicon lateral mode resonators[J]. *Sensors and Actuators A: Physical*, 2017, 259: 144-151.
8. J. Zou, C. -M. Lin, G. Tang, A. P. Pisano. High-Q butterfly-shaped AlN Lamb wave resonators[J]. *IEEE Electron Device Letters*, 2017, 38(12): 1739-1742.
9. Zhu, H.; Lee, J.E.Y. AlN piezoelectric on silicon MEMS resonator with boosted Q using planar patterned phononic crystals on anchors. In Proceedings of the 2015 28th IEEE International Conference on Micro Electro Mechanical Systems (MEMS), *Estoril,Portugal*, 18–22 January 2015; pp. 797–800.

10. Binci, L., Tu, C., Zhu, H., & Lee, E.Y. (2016). Planar ring-shaped phononic crystal anchoring boundaries for enhancing the quality factor of lamb mode resonators. *Applied Physics Letters*, 109(20), 2596-512.
11. Siddiqi, M.W.U.; Lee, J.E. Wide Acoustic Bandgap Solid Disk-Shaped Phononic Crystal Anchoring Boundaries for Enhancing Quality Factor in AlN-on-Si MEMS Resonators. *Micromachines* 2018, 9, 413.
12. Lu R, Manzaneque T, Yang Y, et al. Lithium Niobate Phononic Crystals for Tailoring Performance of RF Laterally Vibrating Devices[J]. *IEEE Transactions on Ultrasonics Ferroelectrics & Frequency Control*, 2018:934-944.
13. Bao, F.-H.; Wu, X.-Q.; Zhou, X.; Wu, Q.-D.; Zhang, X.-S.; Bao, J.-F. Spider web-like phononic crystals for piezoelectric MEMS resonators to reduce acoustic energy dissipation. *Micromachines* 2019, 10, 626.
14. F.-H. Bao, L.-L. Bao, X.-Y. Li, et al. Multi-stage phononic crystal structure for anchor-loss reduction of thin-film piezoelectric-on-silicon microelectromechanical-system resonator[J]. *Applied Physics Express*, 2018, 11(6): 067201.
15. F.-H. Bao, J.-F. Bao, J. E.-Y. Lee, et al. Quality factor improvement of piezoelectric MEMS resonator by the conjunction of frame structure and phononic crystals[J]. *Sensors and Actuators A: Physical*, 2019, 297: 111541.
16. Workie, T.B.; Liu, J.; Wu, Z.; Tang, P.; Bao, J.-F.; Hashimoto, K.-Y. Swastika Hole shaped Phononic Crystal for Quality enhancement of Contour Mode Resonators. *In Proceedings of the 2021 IEEE MTT-S International Wireless Symposium (IWS), Nanjing, China*,23–26 May 2021; pp. 1–3.
17. Ha, T.D.; Bao, J. A phononic crystal strip based on silicon for support tether applications in silicon-based MEMS resonators and effects of temperature and dopant on its band gap characteristics. *AIP Adv*. 2016, 6, 045211.
18. Awad, M.; Workie, T.B.; Bao, J.-F.; Hashimoto, K.-y. Reem-Shape Phononic Crystal for Q Anchor Enhancement of Thin-Film-Piezoelectric-on-Si MEMS Resonator. *Micromachines* 2023, 14, 1540.
19. Ha, T.D.; Bao, J. Reducing anchor loss in thin-film aluminum nitride-on-diamond contour mode MEMS resonators with support tethers based on phononic crystal strip and reflector. *Microsyst. Technol*. 2016, 22, 791–800.
20. Rawat, U.; Nair, D.R.; DasGupta, A. Piezoelectric-on-Silicon array resonators with asymmetric phononic crystal tethering. *J. Microelectromech. Syst*. 2017, 26, 773–781.
21. Khan, M.A.; Bao, J.-F.; Bao, F.-H.; Zhou, X. Concentric Split Aluminum with Silicon-Aluminum Nitride Annular Rings Resonators. Micromachines 2019, 10, 296.
22. Bao, J.; Workie, T.B.; Hashimoto, K.Y. Performance improvement of RF acoustic wave resonators using phononic crystals. In Proceedings of the 2022 IEEE MTT-S International Microwave Workshop Series on Advanced Materials and Processes for RF and THz Applications (IMWS-AMP), Guangzhou, China, 27–29 November 2022; pp. 1–2.
23. Liu, J.; Workie, T.B.; Wu, Z.; Tang, P.; Bao, J.F.; Hashimoto, K.Y. Acoustic Reflectors for Anchor Loss Reduction of Thin Film Piezoelectric on Substrate Resonators. In Proceedings of the 2021 IEEE MTT-S International Wireless Symposium (IWS), Nanjing, China, 23–26 May 2021; pp. 1–3.
24. Chen, P.J.; Workie, T.B.; Feng, J.J.; Bao, J.F.; Hashimoto, K.Y. Four-Leaf Clover Shaped Phononic Crystals for Quality Factor Improvement of AlN Contour Mode Resonator. In Proceedings of the 2022 IEEE International Ultrasonics Symposium (IUS), Venice, Italy, 10–13 October 2022; pp. 1–3.
25. Workie, T.B.; Wu, T.; Bao, J.F.; Hashimoto, K.Y. Design for the high-quality factor of piezoelectric-on-silicon MEMS resonators using resonant plate shape and phononic crystals. Jpn. J. Appl. Phys. 2021, 60, SDDA03.
26. Liu, J.; Workie, T.B.; Wu, T.; Wu, Z.; Gong, K.; Bao, J.; Hashimoto, K.-y. Q-Factor Enhancement of Thin-Film Piezoelectric-on-Silicon MEMS Resonator by Phononic Crystal-Reflector Composite Structure. Micromachines 2020, 11, 1130.
27. Workie, T.B.; Wu, T.; Bao, J.; Hashimoto, K. Q-factor enhancement of MEMS Resonators with Ditetragonal Prism shaped Phononic Crystal (DTP-PnC). In USE; USE 2020|Contents: Osaka, Japan, 2020; Volume 41, p. 2E5-2. Available online: https://www.use-dl.org/2020/proceedings/pdf/2E5-2.pdf.
28. Khelif, A.; Adibi, A. Phononic Crystals: Fundamentals and Applications; *Springer: Berlin/Heidelberg, Germany*, 2015.
29. Torrent D, J Sánchez-Dehesa. Radial wave crystals: radially periodic structures from anisotropic metamaterials for engineering acoustic or electromagnetic waves. *J. Physical Review Letters*, 2009, 103(6):064301.
30. Torrent D, José Sánchez-Dehesa. Acoustic resonances in two-dimensional radial sonic crystal shells[J]. New Journal of Physics, 2010.
31. Spiousas I, Torrent D, Sanchez-Dehesa J. Experimental realization of broadband tunable resonators based on anisotropic metafluids[J]. *Applied Physics Letters*, 2011, 98(24):452.
32. Li Y, Chen T, Wang X, et al. Propagation of Lamb waves in one-dimensional radial phononic crystal plates with periodic corrugations[J]. *Journal of Applied Physics*, 2014,115(5): 054907.
33. Ma T, Chen T, Wang X, et al. Band structures of bilayer radial phononic crystal plate with crystal gliding[J]. *Journal of Applied Physics*, 2014, 116(10): 104505.

 doi:10.20944/preprints202311.1597.v1

34. Shu, Hai Sheng, et al. "Bandgap analysis of cylindrical shells of generalized phononic crystals by transfer matrix method." *International Journal of Modern Physics B* (2015):29-.
35. Shi, Xiaona, et al. "Research on wave bandgaps in a circular plate of radial phononic crystal." *International Journal of Modern Physics B* 30.23(2016):1650162.
36. An, Shuowei, et al. "Band gap characteristics of radial wave in a two-dimensional cylindrical shell with radial and circumferential periodicities." *Aip Advances* 8.3(2018):035110.